Catalysis Today 431 (2024) 114560

Contents lists available at ScienceDirect

Catalysis Today

journal homepage: www.elsevier.com/locate/cattod

Computationally screening non-precious single atom catalysts for oxygen reduction in alkaline media

Tahereh Jangjooye Shaldehi [a], Ling Meng [b], Soosan Rowshanzamir [a,*], Mohammad Javad Parnian [c], Kai Exner [d], Francesc Viñes [b], Francesc Illas [b,*]

[a] Hydrogen & Fuel Cell Research Laboratory, School of Chemical, Petroleum and Gas Engineering, Iran University of Science and Technology, Narmak, Tehran 16846–13114, Iran

[b] Departament de Ciència de Materials i Química Física & Institut de Química Teòrica i Computacional (IQTCUB), Universitat de Barcelona, c/ Martí i Franquès 1–11, 08028 Barcelona, Spain

[c] Department of Chemical and Petroleum Engineering, University of Calgary, 2500 University Dr. NW, Calgary, Alberta T2N 1N4, Canada

[d] University Duisburg-Essen, Faculty of Chemistry, Theoretical Inorganic Chemistry, Universitätsstraße 5, 45141 Essen, Germany; Cluster of Excellence RESOLV, Bochum, Germany; Center for Nanointegration (CENIDE) Duisburg-Essen, Duisburg, Germany

ARTICLE INFO

Keywords:
Oxygen reduction reaction
ORR
Alkaline media
Single atom catalyst
DFT

ABSTRACT

The performance of single-atom catalysts (SACs) containing Sc, Ti, V, Mn, Fe, Ni, Cu, and Pt on N-doped carbon (NC) as possible cathodes in advanced chlor-alkali electrolysis has been investigated by means of density functional theory (DFT) with the aim of finding candidates to improve the sluggish kinetics of the oxygen reduction reaction (ORR). A plausible mechanism is proposed for the ORR that allows making use of the computational hydrogen electrode (CHE) approach in this environment, and suitable models have been used to estimate the free-energy changes corresponding to the elementary reaction steps. The performance of the different catalysts has been analyzed in terms of the electrochemical-step symmetry index (ESSI) and G_{max} descriptors. From these descriptors, the Cu-containing SAC is predicted to exhibit the highest catalytic activity which is consistent with a theoretical overpotential of 0.71 V, indicating that this type of catalysts in oxygen depolarized cathodes (ODCs) may overcome the limitations of the high cost and low abundance of Pt and other precious metals.

1. Introduction

The chlor-alkali industrial process, the second largest electrochemical process after the Hall–Héroult process for Al production, aims at producing gaseous chlorine, sodium, and/or potassium hydroxide by the electrolysis of brine solutions [1–3]. Unfortunately, these processes are energy costly, use mercury electrodes or asbestos-containing membranes with evident concomitant environmental issues, harmful effects, and economic problems [4–8]. Consequently, the petrochemical industry is interested in finding alternative, more sustainable, processes to produce caustic soda and gaseous chlorine. In this sense, the so-called advanced chlor-alkali process [9,10] is one of the latest developed approaches aimed at reducing energy consumption, which is working at the industrial scale. In this process, oxygen depolarized cathodes (ODCs) are used in the membrane electrochemical cell at the cathode to facilitate water formation *via* oxygen reduction reaction (ORR) rather than hydrogen evolution reaction (HER). From a thermodynamic point of view, it is a clear advantage to apply ODCs in membrane electrochemical cells as the equilibrium potential difference between the anode (chlorine evolution) and the cathode is reduced by about 1 V compared to the conventional process with the HER at the cathode [11,12]. Therefore, the use of ODCs in membrane cells easily leads to a 30% saving in energy consumption [13,14].

Being a type of gas diffusion electrodes (GDEs), the ODCs consist of a micro/nano-particule catalyst and a hydrophobic material [15,16]. The reaction site in the ODC involves a three-phase boundary with oxygen, water, and electrons at the gas, liquid, and solid phases, respectively. In the ODCs, the ORR suffers from a sluggish reaction kinetics due to the transfer of four electrons for the reduction of a single oxygen molecule [17]. To enhance the performance of chlor-alkali electrolysis, a suitable electrocatalyst is needed, which is able to catalyze ORR in a sodium hydroxide solution at 80–90 °C. Common catalysts for ODCs are

* Corresponding authors.
E-mail addresses: rowshanzamir@iust.ac.ir (S. Rowshanzamir), francesc.illas@ub.edu (F. Illas).

https://doi.org/10.1016/j.cattod.2024.114560
Received 8 October 2023; Received in revised form 25 January 2024; Accepted 30 January 2024
Available online 3 February 2024

carbon-supported platinum [18–20] and silver [21–23], metal porphyrins, phthalocyanins, and perovskites [24,25].

In the last decades, significant research has been carried out to substitute the highly active but scarce and expensive Pt-based catalysts [26,27]. In particular, non-precious metal catalysts have attracted attention because of their promising ORR activity in electrochemical technologies [28–36]. Among the investigated catalysts, transition metal single-atom catalysts (SACs) are promising in speeding up the slow ORR kinetics with high efficiency and low cost. SACs involve single metal atoms dispersed and anchored on a given substrate, have been used in several electrocatalytic processes, in energy storage [37–42] and have shown high catalytic performance for ORR in acidic or alkaline media [43,44].

The search for active and stable SACs for the ORR involves screening a large number of potential material motifs. To render such screening in an efficient fashion, first principles based theoretical approaches such as density functional theory (DFT) in conjunction with the computational hydrogen electrode (CHE) model [45] have become a powerful tool to predict the electrocatalytic activity of ORR catalysts [46–49]. Nevertheless, most theoretical investigations of the ORR have focused on acid solutions, and only a few studies have been reported on alkaline environments. Yu *et al.* [50] have studied the ORR catalyzed by N-doped graphene on the cathode of fuel cells by DFT calculations and showed that this system is promising to partially replace the conventionally used Pt in the alkaline medium.

For the ORR in alkaline medium, the performance of ODC single-atom electrocatalyst in the chlor- alkali electrolysis has been studied in detail from the experimental point of view [51–55]. However, to properly interpret and understand experimental results, and, more importantly, to predict the properties of new materials before synthesis, a detailed analysis from theory is needed. In this work, the ORR activity in alkaline medium of a selection of non-precious single atoms from the 3d transition series (Sc, Ti, V, Mn, Fe, Ni, Cu) supported on N-doped graphene is explored computationally by means of DFT calculations and the CHE model, including Pt as a reference case.

2. ORR mechanism

The ORR mechanism is complex and includes intermediates that depend on the nature of the electrode, electrocatalyst, electrolyte, and on the pH, with significant differences in the proposed mechanism in acid or alkaline media.

2.1. The ORR mechanism in acid media

In acid media, the overall reaction is.

$$O_2\,(g) + 4\,H^+ + 4e^- \rightarrow 2\,H_2O \tag{1}$$

with an equilibrium potential of U = 1.23 V *vs.* RHE (reversible hydrogen electrode). It is common to postulate that there are three adsorbed intermediates in the pathway from O_2 to H_2O [48,56–60], namely *O, *OH, and *OOH that are formed as in Eqs. 2–5.

$$O_2\,(g) + H^+ + e^- + * \rightarrow *OOH \tag{2}$$

$$*OOH + H^+ + e^- \rightarrow *O + H_2O\,(l) \tag{3}$$

$$*O + H^+ + e^- \rightarrow *OH \tag{4}$$

$$*OH + H^+ + e^- \rightarrow H_2O\,(l) + * \tag{5}$$

where O_2 and H_2O are in the gas and liquid phase, respectively. One must point out that Eqs. (2–5) are reconciled with the "mononuclear ORR mechanism", which is the reverse pathway for the mononuclear OER mechanism. This mechanism is likely operative in the ORR when the respective electrocatalyst binds *OH strongly (left leg of the volcano) as discussed in Ref. [61]. Note also that there are several other mechanistic pathways for ORR feasible, including various chemical and electrochemical steps which make the ORR mechanistic description more complex than originally anticipated, and different mechanistic pathways can be operative for different catalysts.

For reactions (2−5) the changes in Gibbs free energy (ΔG_i, i = 2–5) can be computed as detailed extensively in the literatures [48,62] and briefly reviewed in the next section. The calculated ΔG_i provides an estimate of the equilibrium potential required for each step (E_i^o) to take place on a given substrate simply because $E_i^o = -\frac{\Delta G_i}{e_0}$ where e_0 is the electron charge [45]. Note in addition that, irrespective of the catalyst used, the sum of ΔG_i values must be the − 4.92 eV, the equilibrium Gibbs free energy for the reaction at U = 0 V *vs.* RHE. Therefore, it is believed that an ideal catalyst reveals $\Delta G_i = -1.23$ eV for any i at U = 0 V *vs.* RHE —or $\Delta G_i = 0$ eV for any i at U = 1.23 V *vs.* RHE—, and the maximum deviation from this value defines the theoretical overpotential or limiting potential as explained in detail in the next section [63].

From the preceding discussion, it turns out that from the calculated equilibrium potential one can predict the corresponding overpotential, and thus be able to screen different materials in the search for the improved catalyst. Regarding the estimate of the ΔG_i values, here it suffices to state that for the adsorbed species, the vibrational contribution to entropy is estimated from harmonic frequencies, the free energy of O_2 is taken relative to the experimental H_2O (l) formation free energy —$\Delta G^{f,exp}$ (H_2O)— and H_2O and H_2 gas phase molecules calculated free energies with the entropy contribution taken from thermodynamic tables,

$$G(O_2) = 2(\Delta G^{f,exp}\,(H_2O) - G(H_2O)) - 2\,G(H_2) \tag{6}$$

and that, from the CHE it follows that at $pH = 0$ and 1 bar and 298.15 K.

$$G(H^+ + e^-) = 1/2\,G(H_2) \tag{7}$$

Finally, whenever needed, the free energy of liquid water can be estimated by adding an appropriate entropy correction to the gas phase value [45]. It is worth pointing out that the "mononuclear" mechanism discussed above has been questioned by Barlocco *et al.* [41] who showed that the oxygen evolution reaction (OER) on SACs can follow an alternative pathway. These authors studied a set of 30 SACs involving different carbon-based materials and found that intermediates such as M$(OH)_2$, M(O)(OH), M($O)_2$, and M(O_2), where M stands for the metal atom in the SAC, exhibit larger adsorption free energy and, hence, may play a role in the OER and ORR mechanisms.

2.2. The ORR mechanism in alkaline media

The ORR reaction in alkaline media can be written as in Eq. (8).

$$O_2(g) + 2\,H_2O + 4e^- \rightarrow 4OH^- \tag{8}$$

and its mechanism has been less studied with some issues remaining open. For instance, it is sometimes postulated that the first step is as in Eq. (9).

$$O_2 + e^- + * \rightarrow *O_2^- \tag{9}$$

and that, at high pH values, **OOH* is never formed from a coupled proton-electron transfer (CPET) step [64]. In fact, Smickler *et al.* [65] have argued that the electron transfer in Eq. (9) occurs at the outer sphere which agrees with the fact that the overall reaction takes place a similar speed in different metallic electrodes such a silver and gold. The mechanism that, according to Smickler *et al.* [65] follows from Eq. (9) involves adsorbed charged species which are difficult to accurately model with periodic DFT approaches and makes the overall approach difficult to apply for systematic screening potential electrocatalysts.

Recently, an alternative mechanism has been proposed by Liang *et al.* [66] for the OER in basic media that, while not involving CPET, allows

the use of the CHE model. Since the OER and ORR are reverse processes, the proposed steps for the ORR are as follows:

$$O_2 + * + H_2O + e^- \rightarrow *OOH + OH^- \quad (10)$$

$$*OOH + e^- \rightarrow *O + OH^- \quad (11)$$

$$*O + H_2O + e^- \rightarrow *OH + OH^- \quad (12)$$

$$*OH + e^- \rightarrow OH^- + * \quad (13)$$

which involves the *O, *OH, and *OOH intermediates as in the mononuclear mechanism in acidic media. Now, following the procedure by Liang *et al.* [66], as summarized in the next section, one can compute the change in Gibbs free energy (ΔG_i, $i = 10$–13) and estimate the equilibrium potential of each step, to ultimately predict the theoretical overpotential or other activity descriptors for a given catalyst.

To end up this section, three remarks are necessary. First, note that the ORR reaction as in Eq. (8) is accompanied by the corresponding hydrogen oxidation half reaction $2\,H_2 \rightarrow 4\,H^+ + 4e^-$ for which, at standard conditions, the equilibrium potential *vs.* SHE is taken as zero. Second, one must be aware that alternative mechanisms with different intermediates may need to be considered as discussed in the recent review by Di Liberto and Pacchioni [67]; and third, one should not forget that the models discussed involve some limitations as they neglect the presence of the solvent which may also become an active reaction species [67].

3. Electrode models, theoretical framework, and computational details

As mentioned in the introduction, the focus of the present work is on screening SAC models that can serve as ODC in chlor-alkali electrolyzers. To represent the active sites, we consider graphene-like patch models where a single metal atom is coordinated to four N atoms as indicated in Fig. 1. The models are similar to those used previously by Calle-Vallejo *et al.* [68] but with a considerably larger unit cell. The present model can also be seen as a periodic version of the one used in recent work investigating the chlorine evolution reaction [69]. Thus, a sufficiently large $5 \times 5 \times 1$ supercell of the one-layer pristine graphene is chosen with starting C-C bond length of 1.42 Å as in pristine graphene and lattice parameters of $a = b = 12.3$ Å and $c = 20$ Å, the latter value being chosen to prevent interaction between periodic replicas. Next, the N-doped graphene model was generated by replacing four C with four N atoms and, finally, the SAC model is obtained by adding a metal atom (Sc, Ti, V, Mn, Fe, Ni, Cu, and Pt) to the cavity surrounding the atoms. In this way, the metal atom forms two five- and two six-membered rings, as seen in Fig. 1. The final unit cell contains 44 C atoms, 4 N atoms, and one single metal atom.

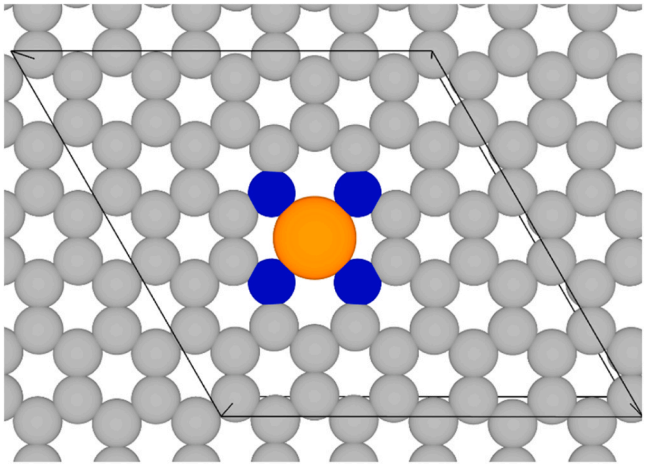

Fig. 1. Schematic representation of the model used to represent the SAC electrocatalysts used in the present work. Grey, blue, and orange balls denote C, N, and the metal atom, respectively.

Herein, we discuss the ORR under alkaline conditions by adapting the mechanism from Liang et *al.* [66]. By using the RHE as a reference electrode under standard conditions of hydrogen gas pressure $p_{H_2} = 1$ bar and $T = 298.15$ K, the necessary ΔG_i ($i = 10$–13) values are calculated as follows:

$$\Delta G_{10} = [G(*OOH) + G(OH^-)] - [G(O_2) + G(*) + G(H_2O) + G(e^-)] \quad (14)$$

$$\Delta G_{11} = [G(*O) + G(OH^-)] - [G(*OOH) + G(e^-)] \quad (15)$$

$$\Delta G_{12} = [G(*OH) + G(OH^-)] - [G(*O) + G(H_2O) + G(e^-)] \quad (16)$$

$$\Delta G_{13} = [G(*) + G(OH^-)] - [G(*OH) + G(e^-)] \quad (17)$$

Following the literature [48,62], G^* is just estimated from the total energy of the clean electrode model, in our case that of the model in Fig. 1, so that G(*) = E*, whereas for the adsorbed species (A = *OOH, *OH, *O).

$$G(\mathrm{A}) = E(\mathrm{A}) + E_{\mathrm{ZPE}}(\mathrm{A}) - TS(\mathrm{A}) \quad (18)$$

where E(A) represents the total energy of the electrode model of Fig. 1 with the adsorbed species A, E_{ZPE}(A) is the corresponding vibrational zero-point energy (ZPE) considering only the adsorbate degrees of freedom, and S(A) stands for the entropy of the adsorbed species which includes the vibrational contribution only. In addition, the chemical potential of O_2 can be obtained by assuming the equilibrium in Eq. (6). The only remaining terms are $G(OH^-)$ and $G(e^-)$ and more precisely their difference, namely $G(OH^-) - G(e^-)$. To calculate this term, we also follow Liang *et al.* [66] who used the equilibrium as in Eq. (19).

$$H_2O(l) \rightarrow H^+ + OH^- \quad (19)$$

for which it holds that.

$$G(OH^-) + G(H^+) = G(H_2O(l)) \quad (20)$$

adding and subtracting $G(e^-)$ in the left-hand side one has.

$$G(OH^-) - G(e^-) + G(H^+) + G(e^-) = G(H_2O(l)) \quad (21)$$

which finally leads to.

$$G(OH^-) - G(e^-) = G(H_2O) - \{G(H^+) + G(e^-)\} = G(H_2O) - 1/2\,G(H_2) \quad (22)$$

Substituting Eq. (22) into Eqs. (14)–(17), one gets.

$$\Delta G_{10} = G(*OOH) - [G(O_2) + G(*) + G(H_2O)] + G(H_2O) - 1/2\,G(H_2) \quad (23)$$

$$\Delta G_{11} = G(*O) - G(*OOH) + G(H_2O) - 1/2\,G(H_2) \quad (24)$$

$$\Delta G_{12} = G(*OH) - [G(*O) + G(H_2O)] + G(H_2O) - 1/2\,G(H_2) \quad (25)$$

$$\Delta G_{13} = G(*) - G(*OH) + G(H_2O) - 1/2\,G(H_2) \quad (26)$$

So far all ΔG values are referred to standard conditions or zero pH and zero potential which is often indicated as $\Delta G(0,0)$. To obtain the corresponding expressions at finite pH and potential relative to the SHE, it suffices to recall that for an elementary step involving a single CPET one can write [70,71].

$$\Delta G(pH, U) = \Delta G(0,0) - \nu(H^+) k_B T (\ln 10) pH - \; - \nu(e^-) eU \quad (27)$$

where e is the elementary charge of an electron and U is the applied electrode potential with respect to the SHE with $\nu(H^+)$ and $\nu(e^-)$ being the number of transferred protons and electrons, respectively. Using Eq. (27) one easily gets the equivalent of ΔG_i, ($i = 10$–13) for a given pH and potential. In acidic conditions, $pH = 0$, we can use SHE or RHE, because.

$$\Delta G(pH, U) = \Delta G(0,0 \quad (28)$$

$$eU(RHE) = eU(SHE) \quad (29)$$

However, under alkaline conditions, *i.e.* at $pH = 14$, then.

$$\Delta G(pH, U) = \Delta G(0,0) - k_B T(\ln 10) pH - eU =$$

$$= \Delta G(0,0) - 0.83 - eU \quad (30)$$

Consequently, for $U = 0$ *vs.* SHE one has $\Delta G(14,U) = \Delta G(0,0) - 0.83$, which simply means that for each elementary reaction step, one just need to subtract 0.83 eV from data in the acidic medium. In other words;

$$eU(RHE) = eU(SHE) - k_B T(\ln 10) pH = eU(SHE) - 0.83 \quad (31)$$

That is, for $\Delta G(pH,U)$ under acidic $pH = 0$ and $U = 0$ V *vs.* SHE, $\Delta G(0,0) = U_0 \times 4 = -1.23$ V (*vs.* SHE) $\times 4 = -4.92$ eV, whereas for alkaline $pH = 14$, $\Delta G(14,0) = U_0 \times 4 = (1.23 - 0.83)$ V (*vs.* SHE) $\times 4 = -1.6$ eV. In the context of the CHE model and for a real catalyst, the highest potential at which all reaction steps are exergonic is termed the thermodynamic limiting potential (U_L) [48] and is defined as

$$U_L = U_0 - \frac{1}{e} \left[\max(\Delta G_i)_{i=10-13}\right] \quad (32)$$

The difference between the equilibrium potential U_0 and the limiting potential (U_L) defines the theoretical overpotential (η_{theo}), this is.

$$\eta_{theo} = U_0 - U_L \quad (33)$$

For the ORR in acidic and alkaline conditions U_0 is + 1.23 V and + 0.4 V *vs.* SHE, respectively. Note also that, for the ideal catalyst, all steps have the same ΔG_i, and U_L matches U_0 leading to $\eta = 0$. It is also important to note that η (as well as U_L) serves as an indicator of the effectiveness of a given catalyst activity and cannot be directly compared to a measured overpotential, which is inherently influenced by the current density.

The set of equations above, similar to those in the original work of Nørskov *et al.* [45] for the reaction in acid media, allows one to predict the potential of each step just from DFT based calculation. At this point, it is worth pointing out that, because of the approximate character of the exchange-correlation functionals, the DFT calculated energy of gas phase molecules suffers from rather large errors which, severely affect the equilibrium potential predictions [63,72]. To a large extent, the DFT intrinsic error can be minimized by means of a semiempirical correction. In the case of the ORR, the error, measured as the Gibbs free energy difference between the experimental (−4.92 eV) and the calculated value for the ideal catalyst is almost entirely due to the energy of the gas phase O_2 molecule and depends on the chosen exchange-correlation functional [63].

The DFT calculations were carried out allowing for spin polarization with the Perdew–Burke–Ernzerhof (PBE) exchange-correlation functional [73], with dispersion effects included through the D3 approach of Grimme [74]. This choice is justified by the good performance of PBE in describing the transition metal series and it provides a good description of closed-shell metallic systems [75–78]. Note in passing that some authors have suggested that the implicit more accurate hybrid functionals or its cheaper PBE+U version provide a slightly different and, hence, expectedly more accurate description of SAC systems of interest in electrocatalysis [79,80]. Nevertheless, one must also be aware of the intrinsic errors of the available functionals in describing the gas phase thermochemistry [81] as reactants and products are gas phase molecules. The gas phase errors of PBE are known and can be corrected as indicated below. Also, using the same method for the different systems permits to catch the main trends which is the main goal of the present work.

The valence electron density was expressed using a plane-wave basis set with a kinetic energy cut-off of 415 eV and the projector augmented wave (PAW) method of Bloch [82], as implemented by Kresse and Joubert [83], was used to account for the effect of the core electrons on the valence electron density. The necessary numerical integrations in the reciprocal space were carried out using a 4 × 4 × 1 mesh of special **k**-points [84]. The optimization of the structures was finalized until the maximum force on any atom in the supercell were all below 0.01 eV $Å^{-1}$. The criterion of convergence of the total energy along the optimization was set to 10^{-5} eV. For the gas phase species, the total energy was obtained by placing it in a large asymmetric box. Finally, *G (O₂)* in Eq. (23), has been corrected by the estimated PBE error of 0.46 eV as reported by Sargeant *et al.* [63], so that the PBE calculated Gibbs free energy for the ORR, for which the PBE value is 4.46 eV, matches the experimental value. All calculations have been carried out using the Vienna *ab initio* simulation package (VASP) [85,86].

4. Stability of the SAC models

It is well-known that transition metal atoms deposited on carbon materials tend to interact ultimately by forming clusters and large nanoparticles, which is detrimental to catalysis and, consequently, reduce their performance. Hence, when investigating possible SACs, it is necessary to first assess their stability. In the present work, we consider formation energy, binding energy, and cohesive energy of the considered models. The formation energy (E_f) of the SAC model can be defined as the energy required to dissociate the catalyst into its individual components, which is directly related to stability, and can be estimated as:

$$E_f = [E_{SAC} + 2\ E_C] - [E_M + E_{CN}] \quad (34)$$

where E_{SAC} and E_{CN} are the total energies of the optimized SAC model in Fig. 1 and the (5 ×5) pristine N-graphene supercell with four appropriately located N atoms; E_C is the energy of the carbon atom calculated from graphene and E_M is chemical potential of M atom calculated from its corresponding bulk structure. The factor 2 in Eq. (34) arises from the fact that two C atoms have to be removed to accommodate the M atom in the SAC. Obviously, the more negative the calculated E_f, the more thermodynamically stable the catalyst is. The E_f values summarized in Table 1 indicate that the SAC models used are thermodynamically stable. The binding energy (E_b) is defined as;.

$$E_b = E_{SAC} - E_{support} - E_M \quad (35)$$

where $E_{support}$ and E_M are the total energies of the SAC model without M atom and single M atom. Comparing the obtained E_b values in Table 1 with the corresponding cohesive energy (E_{coh}) values of the bulk metal (3.90, 4.85, 5.31, 2.92, 4.87, 4.87, 3.48, and 5.50 eV for Sc, Ti, V, Mn, Fe, Ni, Cu, and Pt, respectively), taken from Ref. [76], which were calculated using the same approach, it appears that, in all cases, $E_b > E_{coh}$, clearly indicating that metal sintering is not thermodynamically favored.

To a large extent, the adsorption energy (E_{ads}) of key reaction intermediates such as O_2, OOH, O, and OH determines the magnitude of the Gibbs free energy values that govern the catalytic performance of the ORR, as discussed above. Therefore, it is interesting to analyze the main trends just for the adsorption energy of the different species *X* defined as:

$$E_{ads} = E_{SAC\_X} - E_{SAC} - E_X \quad (36)$$

Table 1
Calculated formation energy (E_f), binding energy (E_b), and cohesive energies (E_{coh}) of the different SAC model in eV. The rightmost column corresponds to the calculated Bader net charges (Q) at the M center in the isolated SAC models.

SAC	E_f	E_b	E_{coh}	Q
Sc	-3.85	-8.54	-4.64	1.82
Ti	-2.05	-8.52	-3.67	1.43
V	-1.51	-7.73	-2.42	1.32
Mn	-2.54	-6.77	-3.85	1.29
Fe	-1.75	-7.68	-2.81	1.08
Ni	-2.48	-7.99	-3.12	0.83
Cu	-0.40	-5.26	-1.78	0.90
Pt	-1.67	-7.81	-2.31	0.72

where E_{SAC_X} and E_X are the total energy of X species adsorbed on the SAC and on the gas phase, respectively, computed in the supercell. Negative E_{ads} values indicate that the adsorption process is energetically favorable. The optimal E_{ads} values were obtained by explicitly considering all different adsorption modes and, for each, carrying out its structural optimization. Fig. 2 and Table S1 summarizes the obtained values including a schematic representation of the final optimized structures. Finally, Table 1 also reports the net Bader charges of the metal atoms in each SAC model, all values are positive indicating that the metal gets partially oxidized with the net charge decreasing from Sc to Cu as expected, the lowest value is for Pt which is includes as reference. This confirms that single metal atoms are suitable active sites that lead to considerable differences in charge transfer between substrates and oxygen molecules. Finally, we briefly discuss the density of states (DOS) and projected DOS (PDOS) of all systems with the corresponding plots reported in Fig. S1. The plots show that all systems exhibit a metallic or nearly metallic character that makes them good candidates for electrode. The plots also show a clear overlap between the metal 3*d* (5*d* for Pt) and the N 2*p* levels due to the strong bonding between the metal atoms and the anchoring N atoms.

5. Gibbs free energy profiles and ORR electrocatalysis performance

Here we analyze the four-electron pathway for the ORR in alkaline condition to determine the SAC with the highest electrocatalytic activity. Fig. 3 shows the free-energy profile for each SAC model at zero potential and $pH = 14$, obtained according to Eqs. (23) to (26), and includes the values for the ideal catalyst for comparison. For completeness, the calculated E, E_{ZPE}, TS, and G values for *OOH, *OH, *O on each metal are reported in Tables S2 to S4, respectively. The steps with a positive ΔG value are thermodynamically hindered and determine the theoretical overpotential [87,88]. Fig. S2 shows that in the case of Sc, there is only one step with positive ΔG that corresponds to *O to *OH conversion. For V, Ti, Fe, and Mn, there are two steps with positive ΔG but again with the *O to *OH conversion is thermodynamically most uphill, and thus, defines the potential-determining step (PDS). Interestingly, for Ni, Cu, and Pt, there is only one step with positive ΔG, but it corresponds to *OOH formation as the PDS.

At $pH = 14$, the equilibrium ΔG_{ORR} at $U = 0$ V is -1.60 eV —*i.e.* -0.40×4— as opposite to $\Delta G_{ORR} = -4.92$ eV from -1.23×4 at $pH = 0$. Thus, at $pH = 14$, the equilibrium potential *vs.* SHE is $U = 0.4$ V and, under this condition, ΔG_{ORR} becomes obviously zero as from Eq. (27) it turns out that Gibbs adsorption energies are shifted by $+n_eU$, depending on the number of electrons corresponding to each step. Obviously, for all catalysts, $\Delta G_{ORR} = 0$ eV is met a $U = 0.4$ V *vs.* SHE and $pH = 14$. One must note that, for the ideal catalyst at $U = 0.4$ V *vs.* SHE and $pH = 14$, the four steps have $\Delta G_i = 0$. However, for real catalysts under these conditions, the respective ΔG_i values of the elementary steps are not zero and one needs to consider the limiting potential —U_L as defined in Eq. (32) —, that is, the specific value for each system at which the Gibbs free energies in each electrochemical step become thermoneutral or negative. The calculated U_L values of Sc, Ti, V, Mn, Fe, Ni, Cu, and Pt are -2.91, -3.05, -2.39, -0.47, -0.35, -0.35, -0.31, and -0.69 V, *vs.* SHE, respectively. According to Eq. (32), the difference between the equilibrium potential ($U = 0.4$ V *vs.* SHE) and the limiting potential (U_L) defines the theoretical overpotential η_{theo} —*cf.* Eq. (33)— with values of 3.30, 3.45, 2.79, 0.87, 0.81, 0.75, 0.71, and 1.09 V *vs.* SHE, in the same order, respectively. From this set of results, it is clear that transition metal with few *d* electrons exhibit large limiting potential and this decreases drastically once the d shell is half filled with Cu being identified as the best candidate among the considered SAC systems.

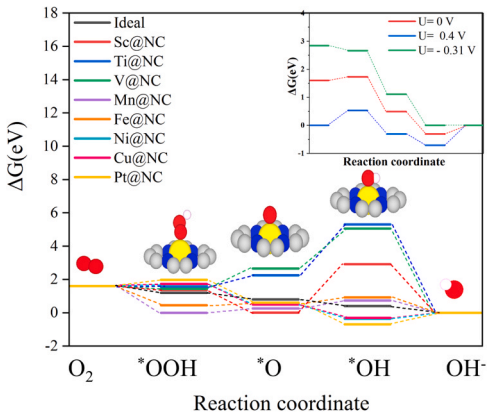

Fig. 3. Gibbs free energy diagrams for ORR at $U = 0$ V and $pH = 14$ for the Sc, Ti, V, Mn, Fe, Ni, Cu, and Pt SACs with the ideal catalysts included for comparison. The inset corresponds to the plots for the Cu SAC at $pH = 14$ and $U = 0$ V, at the equilibrium potential (0.4 V) and at U_L V *vs.* SHE, which is system dependent. Inset images colour-coding as in Fig. 2.

To reach a deeper insight into the mechanism, we explored the electrochemical-step symmetry index (*ESSI*) [89] which allows concluding how close a catalyst is to the ideal case [90,91]. For convenience, the *ESSI* is usually defined for the OER as

$$ESSI = \frac{1}{n}\sum_{1}^{n}\left(\frac{\Delta G_i^{+}}{e^{-}} - E^{0}\right) \quad (37),$$

where ΔG_i^{+} corresponds to the opposite of reaction energies in Eqs. (23–26) larger or equal than the equilibrium potential E^0as only the corresponding steps can be potential-limiting; recall that at the present

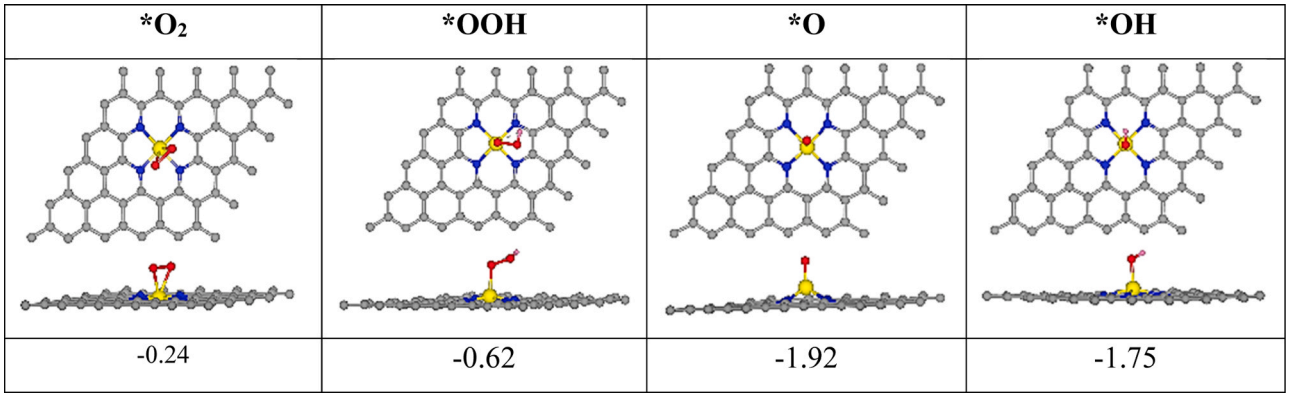

Fig. 2. Top (top) and side (bottom) atomic structures for $*O_2$, *OOH, *O, and *OH at the Cu SAC catalyst with their corresponding adsorption energy (E_{ads}, in eV). The information for the rest of systems can be found in Table S1. O and H atoms are shown as red and white spheres, respectively, while the rest of the color-coding is as in Fig. 1.

alkaline conditions, E^0 is + 0.4 V *vs.* SHE. Obviously, for the ideal catalyst, $n = 4$, $\Delta G_i^+/e^- = E^0$ for all steps i, and thus, *ESSI* = 0 V. The relationship between the *ESSI* for the OER and ORR, hereafter denoted as *ESSI(OER)* and *ESSI(ORR)* has been previous derived by Govindarajan *et al.* [92], so here it suffices to state that for $n = 3, 2, 1$ in the OER one has $n = 1, 2, 3$ in the ORR and *ESSI(ORR)* = −3 *ESSI(OER)*, *ESSI (ORR)* = - *ESSI(OER)* and *ESSI(ORR)* = −1/3 *ESSI(OER)*; note that the case of n = 4 corresponds to the ideal catalysts and one has *ESSI(ORR)* = *ESSI(OER)* = 0. Now let us know, discuss the *ESSI(ORR)* values for the present systems which are also collected in Table 3. For the case of Cu, from Eqs. (23) to (26) one has $\Delta G_{10} = 0.13$ eV, $\Delta G_{11} = -1.24$ eV, $\Delta G_{12} = -0.80$ eV, and $\Delta G_{13} = 0.31$ eV. In this case there are two steps with ΔG smaller than − 0.4 eV, so $n = 2$, either in OER or ORR, and *ESSI (ORR)* = (−1.24 - 0.80)/2 + 0.4 = - 0.62 V. For the case of Ti, $\Delta G_{10} = -0.04$ eV, $\Delta G_{11} = 0.69$ eV, $\Delta G_{12} = 3.05$ eV, and $\Delta G_{13} = -5.30$ eV, here for the OER $n = 1$ therefore, *ESSI(ORR)* = 1/3 [(−5.30/1) + 0.4] = −1.63. Next, in Fig. 4, we plot *ESSI(ORR)* against $-\eta_{ORR}$ and note that, from Table 2, *n* for ORR is equal to 2 for Sc, Mn, Fe, Ni, Cu, Pt while it appears to be 1 for Ti and V. Clearly, catalysts with $n = 2$ displayed low values of η_{ORR} and are close to the ideal catalyst thus supporting previous findings for other systems [91].

To end up the discussion on the obtained results, we briefly comment on the so-called $G_{max}(\eta)$ descriptor [93,94] defined as the largest positive span for all possible reactions between the intermediate species in the mechanism corresponding to Eqs. (10)-(13). This implies computing the Gibbs free energy spans from all possible starting reactants or intermediates to the next ones in the reaction mechanism. Here, one starts by computing the Gibbs free energy from $O_{2(g)}$ to *OOH, *O, *OH or OH^-, and the next step involves computing the Gibbs free energy from *OOH to *O, *OH or OH^-. It continues by computing the Gibbs free energy from *O to *OH or OH^-, and, finally, computing the Gibbs free energy from *OH or OH^-. $G_{max}(\eta)$ just corresponds to the largest of all these values, *i.e.* the largest span. For a more detailed discussion, the reader is referred to reference [95]. For instance, for Sc $G_{max}(\eta)$ at $U = 0$ and $pH = 14$ is determined by ΔG_{12} while for Ti, V, Mn and Fe it is determined by $\Delta G_{11} + \Delta G_{12}$, by ΔG_{13} for Ni and; finally by $\Delta G_{10} + \Delta G_{13}$ for Cu and Pt. Thus, the $G_{max}(\eta)$ values can be directly obtained from the values in Table 2 but are reported in Table 3 for convenience. In principle, high activity is associated to small $G_{max}(\eta)$ values but contrarily, to ESSI, a precise value for the ideal catalyst cannot be defined. From the values in Table 2 and, especially from the plot in Fig. 4, one readily see that the two descriptors lead to a similar description even in ESSI is based on thermodynamics and $G_{max}(\eta)$ comes from the span model proposed by Kozuch and Shaik [96] on the basis of kinetics arguments. In fact, the span governing $G_{max}(\eta)$ provides an approximation of the rate-determining step if a suitable value for the Tafel slope (typically 40 mV/dec or 120 mV/dec) is adopted.

Table 2
Calculated Gibbs free energies (ΔG_i, i = 10–13, in eV), the overpotentials (η), and the limiting potentials (U_L) of different catalysts at $U = 0$ V, $pH = 14$.

SAC	ΔG_{10}	ΔG_{11}	ΔG_{12}	ΔG_{13}	η_{theo} (V)	U_L (V)
Ideal	-0.40	-0.40	-0.40	-0.40	0.00	0.00
Sc	-0.23	-1.35	2.90	-2.92	3.30	-2.90
Ti	-0.04	0.69	3.05	-5.30	3.45	-3.05
V	-0.17	1.23	2.39	-5.05	2.79	-2.39
Mn	-1.61	0.27	0.47	-0.73	0.87	-0.47
Fe	-1.15	0.07	0.41	-0.93	0.81	-0.41
Ni	0.09	-1.07	-0.97	0.35	0.75	-0.35
Cu	0.13	-1.24	-0.8	0.31	0.71	-0.31
Pt	0.37	-1.37	-1.29	0.69	1.09	-0.69

Table 3
Electrochemical-step symmetry index (*ESSI*) and $G_{max}(\eta)$ descriptor for the explored systems at $U = 0$ V and $pH = 14$.

SAC	*ESSI* (V)	G_{max} (η) (eV)
Ideal	0.00	—
Sc	-1.73	2.90
Ti	-1.63	3.74
V	-1.55	3.62
Mn	-0.77	0.74
Fe	-0.64	0.48
Ni	-0.62	0.35
Cu	-0.62	0.44
Pt	-0.93	1.06

6. Conclusions

In the present work, we studied the ORR performance of a series of single-atom catalysts (Sc, Ti, V, Mn, Fe, Ni, Cu, and Pt) in alkaline media as possible candidates for cathodes in advanced chlor-alkali electrolysis, in which the single atoms being anchored at the hollow sites of N-doped graphene. Using periodic density functional theory calculations on a suitable supercell, a four-electron mechanism is proposed that allows studying the Gibbs free-energy profiles and deriving the thermodynamic overpotential invoking the computational hydrogen electron model. The

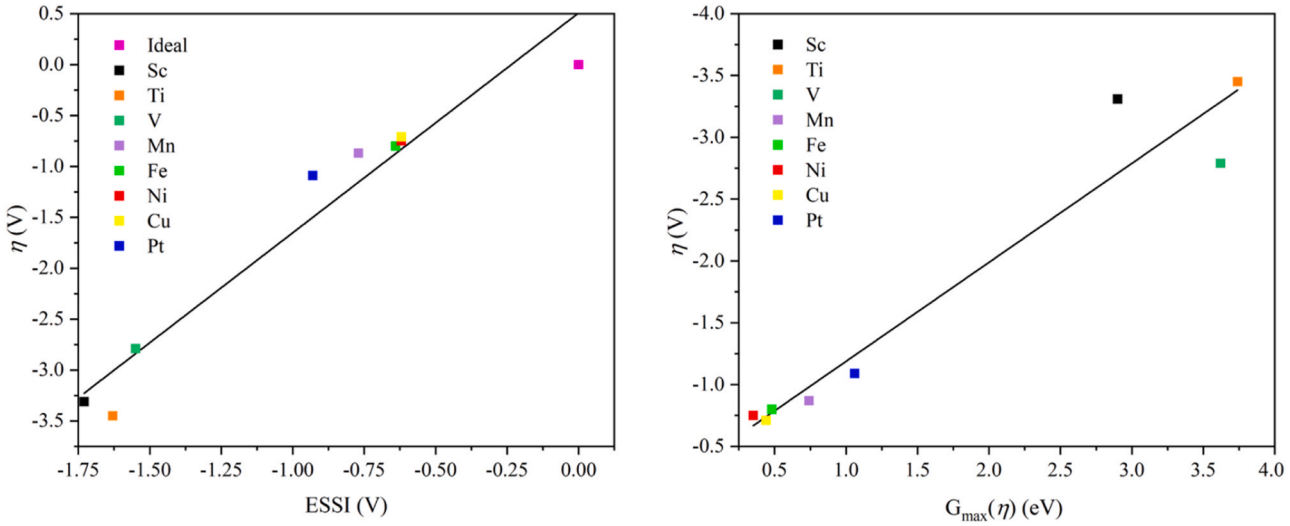

Fig. 4. Plot of predicted overpotentials (η) *versus* the electrochemical-step symmetry index (*ESSI*) for the ORR reaction at U = 0 V and $pH = 14$ (left panel) and *vs.* the $G_{max}(\eta)$ descriptor in eV (right panel). The ideal catalyst, for which η_{ORR} = ESSI = 0 is shown for comparison.

present results show that the N-doping and vacancy effect can create a strong bond between the metal and the substrate. The studied catalysts are stable against sintering with the metal atoms being partially oxidized. From all metals, Cu is predicted to exhibit the best performance with a relatively low theoretical overpotential of 0.71 V in alkaline condition ($pH = 14$). The electrochemical-step symmetry index (ESSI) has been obtained for the ORR in the different systems and plotted against the overpotential. The plot evidences that catalysts with more than one step above the equilibrium potential approach the conditions of the ideal catalysts, in agreement with previous findings for a variety of systems and putting this index as an excellent descriptor of the catalytic activity. This work not only enhances our understanding of graphene-based single-atom catalysts for ORR in alkaline media but also provides an example of the rational design of high-performance ORR catalysts using DFT calculations and theory derived descriptors.

CRediT authorship contribution statement

Shaldehi Tahereh Jangjooye: Data curation, Investigation, Writing – original draft, Formal analysis, Validation. **Rowshanzamir Soosan:** Funding acquisition, Supervision, Writing – review & editing. **Meng Ling:** Conceptualization, Data curation, Formal analysis, Methodology, Writing – original draft, Writing – review & editing, Validation, Visualization. **Exner Kai:** Conceptualization, Formal analysis, Investigation, Methodology, Writing – review & editing, Supervision. **Parnian Mohammad Javad:** Supervision, Writing – review & editing. **Illas Francesc:** Conceptualization, Formal analysis, Funding acquisition, Investigation, Methodology, Resources, Supervision, Writing – original draft, Writing – review & editing, Validation. **Viñes Francesc:** Supervision, Validation, Writing – review & editing, Conceptualization, Investigation, Methodology, Resources.

Declaration of Competing Interest

The authors declare that they have no known competing financial interests or personal relationships that could have appeared to influence the work reported in this paper.

Data availability

Data will be made available on request.

Acknowledgments

The authors are thankful to Dr. Federico Calle-Vallejo for fruitful discussions regarding the electrochemical-step symmetry index. The present study has been supported by the Spanish MCIN/AEI/10.13039/501100011033 PID2021–126076NB-I00 and TED2021–129506B-C22 projects, funded partially by FEDER, *una manera de hacer Europa*, and *María de Maeztu* CEX2021–001202-M grants, including funding from European Union. In addition, the work has been supported in part by COST Action CA18234 and the *Generalitat de Catalunya* financial support to research groups grant 2021SGR79. K.S.E. acknowledges funding by the Ministry of Culture and Science of the Federal State of North Rhine-Westphalia (NRW Return Grant). K.S.E. is associated with the CRC/TRR247: "Heterogeneous Oxidation Catalysis in the Liquid Phase" (Project number 388390466-TRR 247), the RESOLV Cluster of Excellence, funded by the Deutsche Forschungsgemeinschaft under Germany's Excellence Strategy – EXC 2033 – 390677874 – RESOLV, and the Center for Nanointegration (CENIDE). T. Jangjooye Shaldehi special thanks to the Ministry of Science, Research and Technology (MSRT) of the Islamic Republic of Iran for financing her research visit; L.M. thanks the China Scholarship Council (CSC) for financing her PhD (CSC202108390032; and F.V. thanks the ICREA Academia Award 2023 Ref. Ac2216561.

Appendix A. Supporting information

Supplementary data associated with this article can be found in the online version at doi:10.1016/j.cattod.2024.114560.

References

[1] K. Li, Q. Fan, H. Chuai, H. Liu, S. Zhang, X. Ma, Trans. Tianjin Univ. 27 (2021) 202–216.
[2] Y. Liu, Y. Wang, S. Zhao, J. Curr. Opin. Electrochem 37 (2023) 101202.
[3] S. Lakshmanan, T. Murugesan, J. Clean. Technol. Environ. Policy 16 (2014) 225–234.
[4] J.A. Rosales-Huamani, Z.M. Diaz-Cordova, J.A. Montaño-Pisfil, J. Batteries 7 (2021) 1–11.
[5] T.F. O'Brien, T.V. Bommaraju, F. Hine, Handb. Chlor-Alkali Technol. (2005) 17–36.
[6] P. Millet, Handb. Membr. React. 2 (2013) 384–415.
[7] J. Crook, A. Mousavi, J. Environ. Forensics 17 (2016) 211–217.
[8] M. Paidar, V. Fateev, K. Bouzek, J. Electrochim. Acta 209 (2016) 737–756.
[9] J. Jung, S. Postels, A. Bardow, J. Clean. Prod. 80 (2014) 46–56.
[10] Y. Kiros, M. Pirjamali, M. Bursell, J. Electrochim. Acta 51 (2006) 3346–3350.
[11] T. Morimoto, K. Suzuki, T. Matsubara, N. Yoshida, J. Electrochim. Acta 45 (2000) 4257–4262.
[12] M. Sudoh, T. Kondoh, N. Kamiya, T. Ueda, K. Okajima, J. Electrochem. Soc. 147 (2000) 3739.
[13] J. Kintrup, M. Millaruelo, V. Trieu, A. Bulan, E.S. Mojica, J. Electrochem. Soc. 26 (2017) 73–76.
[14] I. Moussallem, J. Jörissen, U. Kunz, S. Pinnow, T. Turek, J. Appl. Electrochem 38 (2008) 1177–1194.
[15] A. Botz, J. Clausmeyer, D. Öhl, T. Tarnev, D. Franzen, T. Turek, W. Schuhmann, J. Angew 57 (2018) 12285–12289.
[16] F. Kubannek, T. Turek, U. Krewer, J. Chem. -Ing. -Tech. 91 (2019) 720–733.
[17] W.S.A. Ignaczak, R. Nazmutdinov, A. Goduljan, L.M. de Campos Pinto, F. Juarez, P. Quaino, E. Santos, J. Nano, Energy 29 (2016) 362–368.
[18] N. Ramaswamy, S. Mukerjee, J. Adv. Phys. Chem. 2012 (2012) 491604.
[19] T.R. Ralph, M.P. Hogarth, J. Platin. Met. Rev. 46 (2002) 3–14.
[20] F. Farzami, E. Joudaki, S.J. Hashemi, J. Eng. 3 (2011) 836–841.
[21] Y. Kiros, T. Quatrano, P. Bj, J. Electrochem Commun. 6 (2004) 526–530.
[22] N. Furuya, H. Aikawa, J. Electrochim. Acta 45 (2000) 4251–4256.
[23] F. Bienen, M. Paulisch, T. Mager, J. Osiewacz, M. Nazari, M. Osenberg, B. Ellendorff, Th Turek, U. Nieken, I. Manke, K. Friedrich, J. ELSA 3 (2022) 1–12.
[24] Y. Kiros, M. Pirjamali, M. Bursell, J. Electrochim. Acta 51 (2006) 3346–3350.
[25] Y. Kiros, M. Bursell, Int. J. Electrochem 3 (2008) 444–451.
[26] M.G. Hosseini, P. Zardari, J. Appl. Surf. Sci. 345 (2015) 223–231.
[27] F. Farzami, E. Joudaki, S.J. Hashemi, J. Eng. 3 (2011) 836–841.
[28] P. Zardari, M.G. Hosseini, Int. J. Hydrog. Energy 41 (2016) 8803–8818.
[29] M.G. Hosseini, P. Zardari, I. Ariankhah, J. Iran. Chem. Soc. 16 (2019) 1749–1760.
[30] K. Fujimoto, Y. Ueda, T. Ishida, Y. Fujii, M. Nakayama, J. Electrochem. Soc. 168 (2021) 086510.
[31] X. Zhai, W. Yang, M. Li, G. Lv, J. Liu, X. Zhang, J. Carbon 65 (2013) 277–286.
[32] A. Zhao, J. Masa, W. Schuhmann, W. Xia, J. Phys. Chem. C. 117 (2013) 24283–24291.
[33] Y. Liang, Y. Li, H. Wang, H. Dai, J. Am. Chem. Soc. 44 (2013) 2013–2036.
[34] J. Schosseler, A. Trentmann, B. Friedrich, K. Hahn, H. Wotruba, J. Met 9 (2019).
[35] U. Tylus, et al., J. APPL CATAL B-ENVIRON 198 (2016) 318–324.
[36] T. Domga, G.B. Noumi, M.J. Sieliechi, J.B. Tchatchueng, J. Carbon Trends 4 (2021) 100043.
[37] L. Jiao, H.L. Jiang, J. Chem. 5 (2019) 786–804.
[38] H. Huang, K. Shen, F. Chen, Y. Li, J. ACS Catal. 10 (2020) 6579–6586.
[39] S. Dang, Q.L. Zhu, Q. Xu, J. Nat. Rev. Mater. 3 (2017).
[40] Y. Shang, X. Duan, S. Wang, Q. Yue, B. Gao, X. Xu, J. CCL 33 (2022) 663–673.
[41] I. Barlocco, L.A. Cipriano, G. Di Liberto, G. Pacchioni, J. Catal. 417 (2023) 351–359.
[42] S. Tosoni, G. Di Liberto, I. Matanovic, G. Pacchioni, J. Power Sources 556 (2023) 232492.
[43] P. Jiao, Sh Wu, C. Zhu, D. Ye, C. Qin, C. An, N. Hu, Q. Deng, J. Nanoscale 14 (2022) 14322–14340.
[44] Y. Wang, F. Hu, Y. Mi, C. Yan, S. Zhao, J. Chem. Eng. 406 (2020) 127135.
[45] J.K. Nørskov, J. Rossmeisl, A. Logadottir, L. Lindqvist, J.R. Kitchin, T. Bligaard, H. Jónsson, J. Phys. Chem. B 108 (2004) 17886–17892.
[46] C. Fu, C. Liu, T. Li, X. Zhang, F. Wang, J. Yang, Y. Jiang, P. Cui, H. Li, J. Comput. Mater. Sci. 170 (2019) 109202.
[47] S. Maheshwari, Y. Li, N. Agrawal, M.J. Janik, Adv. Catal. 63 (2018) 117–167.
[48] A. Kulkarni, S. Siahrostami, A. Patel, J.K. Nørskov, J. Chem. Rev. 118 (2018) 2302–2312.
[49] H.Y. Zhuo, X. Zhang, J.X. Liang, Q. Yu, H. Xiao, J. Li, J. Chem. Rev. 120 (2020) 12315–12341.
[50] L. Yu, X. Pan, X. Cao, P. Hu, X. Bao, J. Catal. 282 (2011) 183–190.
[51] M.G. Hosseini, F. Hosseinzadeh, P. Zardari, M. Darbandi, Int. J. Hydrog. Energy 46 (2021) 28513–28526.
[52] M.G. Hosseini, P. Zardari, J. Appl. Surf. Sci. 345 (2015) 223–231.
[53] M.G. Hosseini, P. Zardari, Int. J. Hydrog. Energy 41 (2016) 8803–8818.
[54] R.S. Figueiredo, R. Bertazzoli, C.A. Rodrigues, J. Ind. Eng. Chem. 52 (2013) 5611–5615.

[55] M.G. Hosseini, F. Hosseinzadeh, P. Zardari, O. Mermer, J. Fuller Nanotub Car N. 26 (2018) 675–687.
[56] X. Zhao, Y. Liu, J. Am. Chem. Soc. 143 (2021) 9423–9428.
[57] S. Siahrostami, G.L. Li, V. Viswanathan, J.K. Nørskov, J. Phys. Chem. Lett. 8 (2017) 1157–1160.
[58] V. Viswanathan, H.A. Hansen, J.K. Nørskov, J. Phys. Chem. Lett. 6 (2015) 4224–4228.
[59] C. Zhang, S. Yu, Y. Xie, W. Zhang, K. Zheng, N.E. Drewett, S.J. Yoo, Z. Wang, L. Shao, H. Tian, J.-G. Kim, W. Zheng, J. Carbon 149 (2019) 370–379.
[60] C. Zhang, W. Zhang, S. Yu, D. Wang, W. Zhang, W. Zheng, M. Wen, H. Tian, K. Huang, S. Feng, J.J. Bentzen, J. ChemElectroChem 4 (2017) 1269–1273.
[61] K. Exner, ChemCatChem 15 (2023) e202201222.
[62] I. Man, H. Su, F. Calle-Vallejo, H. Hansen, J. Martínez, N. Inoglu, J. Kitchin, T. Jaramillo, J. Nørskov, J. Rossmeisl, J, Chemcatchem 3 (2011) 1159–1165.
[63] E. Sargeant, F. Illas, P. Rodríguez, F. Calle-Vallejo, J. ChemElectroChem 896 (2021) 115178.
[64] M.T.M. Koper, J. Chem. Sci. 4 (2013) 2710–2723.
[65] A. Ignaczak, R. Nazmutdinov, A. Goduljan, L.Moreira de Campos Pinto, F. Juarez, P. Quaino, G. Belletti, E. Santos, W. Schmickler, J. Electro 8 (2017) 554–564.
[66] Q. Liang, G. Brocks, A. Bieberle-Hütter, J. Phys. Energy 3 (2021) 026001.
[67] G. Di Liberto, G. Pacchioni, Adv. Mater. 35 (2023) 2307150.
[68] F. Calle-Vallejo, J.I. Martínez, J.M. García-Lastra, E. Abad, M.T.M. Koper, J. Surf, Sci 607 (2013) 47–53.
[69] J. Cho, T. Lim, H. Kim, L. Meng, J. Kim, J.H. Lee, G.Y. Jung, F. Viñes, F. Illas, K. S. Exner, S.H. Joo, C.H. Choi, Nat. Commun. 14 (2023) 3233.
[70] K.S. Exner, J. Anton, T. Jacob, Electrochim. Acta 120 (2014) 460–466.
[71] M. López, K.S. Exner, F. Viñes, F. Illas, Adv. Theory Simul. 6 (2023) 2200217.
[72] L. Granda-Marulanda, A. Rendon-Calle, S. Builes, F. Illas, F. Calle-Vallejo, M.T. M. Koper, ACS Catal. 10 (2020) 6900–6907.
[73] J.P. Perdew, K. Burke, M. Ernzerhof, Rev. Lett. 77 (1996) 3865.
[74] S. Grimme, J. Antony, S. Ehrlich, H. Krieg, J. Chem. Phys. 132 (2010) 154104.
[75] P. Janthon, S. Luo, S.M. Kozlov, F. Viñes, J. Limtrakul, D.G. Truhlar, F. Illas, J. Chem. Theory Comput. 10 (2014) 3832–3839.
[76] P. Janthon, S.M. Kozlov, F. Viñes, J. Limtrakul, F. Illas, J. Chem. Theory Comput. 9 (2013) 1631–1640.
[77] L. Vega, F. Viñes, J. Comput. Chem. 41 (2020) 2598–2603.
[78] D. Vázquez-Parga, A. Fernández-Martínez, F. Viñes, J. Chem. Theory Comput. 19 (2023) 198285–198292.
[79] I. Barlocco, L.A. Cipriano, G. Di Liberto, G. Pacchioni, Adv. Theory Simul. 6 (2023) 2200513.
[80] G. Di Liberto, L.A. Cipriano, G. Pacchioni, A CS Catal. 12 (2022), 5846−585.
[81] R. Urrego-Ortiz, S. Builes, F. Illas, F. Calle-Vallejo, EES Catal. 2 (2024) 157–179.
[82] P.E. Blöch, J. Phys. Rev. B 50 (1994) 17953.
[83] G. Kresse, D. Joubert, J. Phys. Rev. B 59 (1999) 1758.
[84] H.J. Monkhorst, J.D. Pack, J. Phys. Rev. B 13 (1976) 5188.
[85] G. Kresse, J. Furthmuller, Phys. Rev. B Condens. Matter Mater. Phys. 54 (1996) 11169.
[86] J.P. Perdew, K. Burke, M. Ernzerhof, J. Phys. Rev. Lett. 77 (1996) 3865.
[87] M.T.M. Koper, J. Solid, State Electrochem 17 (2013) 339–344.
[88] J.K. Nørskov, J. Rossmeisl, A. Logadottir, L. Lindqvist, J.R. Kitchin, T. Bligaard, H. Jónsson, J. Phys. Chem. B 108 (2004) 17886–17892.
[89] N. Govindarajan, J.M. García-Lastra, E.J. Meijer, F. Calle-Vallejo, Curr. Opin. Electrochem.. 8 (2018) 110–117.
[90] O. Piqué, F. Illas, F. Calle-Vallejo, J. Phys. Chem. Chem. Phys. 22 (2020) 6797–6803.
[91] E. Romeo, F. Illas, F. Calle-Vallejo, J. Chem. Sci. 14 (2023) 3622–3629.
[92] N. Govindarajan, J.M. García-Lastra, E.Jan Meijer, F. Calle-Vallejo, J. Curr. Opin. Electrochem 8 (2018) 110–117.
[93] K. Exner, ACS Catal. 10 (2020) 12607–12617.
[94] S. Razzaq, K. Exner, J. ACS Catal. 13 (2023) 1740–1758.
[95] K.S. Exner, ACS Phys. Chem. Au 3 (2023) 190–198.
[96] S. Kozuch, S. Shaik, J. Acc. Chem. Res. 44 (2011) 101–110.